Check for updates

Silicon nitride programmable photonic processor with folded heaters

Daniel Pérez-López,[1,2,*] **Ana Gutiérrez,**[1] **and José Capmany**[1,2]

[1]*Photonics Research Labs, Universitat Politècnica de València, Camino de Vera, S/N, Valencia, Spain*
[2]*iPronics Programmable Photonics S. L, Valencia, Spain*
*dperez@iteam.upv.es

Abstract: General-purpose programmable photonic processors rely on the large-scale integration of beamsplitters and reconfigurable phase shifters, distributed within unit cells or photonic gates. With their future evolution threatened by several hardware constrains, including the integration density that can be achieved with current mesh topologies, in this work, we present a unit cell topology design to increase the integration density of waveguide mesh arrangements based on folded Mach-Zehnder Interferometers. We report the design details of a 40-unit cell waveguide mesh integrated in a 11mm x 5.5 mm silicon nitride chip achieving, to the best of our knowledge, the highest integration density reported to date for a general-purpose photonic processor. The chip is electrically interfaced to a PCB and we report examples of reconfigurable optical beamsplitters, basic tunable microwave photonic filters with high peak rejection (40 dB approx.), as well as the dynamic interconnection and routing of 5G digitally modulated signals within the photonic mesh.

1. Introduction

Multipurpose programmable photonic integrated circuits aim at configuring arbitrary circuits employing a large-scale set of integrated beamsplitters and phase actuators orchestrated by software programming methods [1–9] Programming complex and versatile circuits demands the integration of a large number of programmable unit cells (PUCs) and the optimization of the performance of their basic unit cells: optical loss, optical crosstalk, tuning crosstalk, footprint and power consumption. Programmable integrated circuits have a wide range of operation fields with reported applications in quantum computing [10–14], Artificial intelligence [15–17], mode unscrambling [18], photonic switching [19], microwave photonics [20,21] and field programmable gate arrays [22].

The design of programmable photonic processors in silicon nitride provide a set of advantages such as low-loss propagation loss, the possibility of working at a wide range of optical wavelengths, and the enhanced temperature stability compared to a silicon on insulator platform [2,23–25]. However, the most basic phase tuning effect available in this platform, the thermo-optic effect, is one order of magnitude weaker than in the silicon counterpart [3,26,28]. The combination of longer bend radius and phase actuators reduces the integration density and, in turn, the versatility of programmable photonic circuits. This issue affects especially hexagonal arrangements, where the void area between unit cells increases with the longitudinal dimension of its unit cells [27]. Earlier attempts to increase the integration density proposed the translation of conventional waveguide mesh arrangements [2,3,27] into compact and flattened designs [29]. Although flattened designs enable an extra design freedom and higher integration densities, silicon nitride platform calls for the search of additional solutions, since the low-confinement, high bend radius and long heater sections result in designs with a reduced number of unit cells.

In this paper, we present a unit cell topology design that increases the integration density of waveguide mesh arrangements. We report design details, characterization, and basic application

of a 40-unit cell waveguide mesh integrated in silicon nitride platform [25], electrically interfaced to a Printed Circuit Board (PCB). We reconfigure the chip to demonstrate different photonic and microwave photonic applications, including reconfigurable optical beamsplitters, ring resonators and Mach-Zehnder interferometers optical filters, microwave photonic filters, as well as the reconfigurable optical routing of 5G signals over the waveguide mesh arrangement.

2. Chip design

Waveguide meshes enable the synthesis of different Photonic Integrated Circuits (PICs) in a common hardware platform by suitable programming each PUC that build up the mesh [1–9]. Most of the reported works to date employ a basic Mach-Zehnder architecture as a PUC [1–9] or a dual-drive directional coupler [23]. By applying a phase shift in one of the arms or the PUC (or differential phase shift), it is possible to tune the splitting ratio of the signal, whereas a common drive of the two phase-shifters leads to a common phase shift modification at the output without altering the splitting ratio. This basic operation, when combined with multiple unit cells, enables the definition of the circuit topology and design parameters of reconfigurable programmable circuits.

2.1. Programmable unit cell design

Most of the reported MZI-based PUC or tunable basic uUnit (TBU) architectures rely on phase shifters describing a straight line over the longitudinal length of the thermo-optic heater. This design is space consuming for hexagonal, square and triangular mesh distributions, and reduces the integration density [27]. As a solution, we propose here a MZI with a folded heater (See Fig. 1(a)), that allows us to squeeze the PUC in the longitudinal dimension and fill the gaps present within the waveguide mesh more uniformly (as it is shown in Fig. 1(b), 1(c), 1e). Moreover, the heat flow of one side of the heater can impose a beneficial thermal crosstalk to the second half of the heater, thus reducing its power consumption. Based on previous simulations and experiments [3,28] the distance of 120 um between arms involves a positive thermal crosstalk contribution of around 3% for each waveguide. This effect could be exacerbated if the design is modified to get the waveguides closer [28]. As a trade-off, the distance reduction between PUCs might increase the inter-PUC tuning crosstalk. To mitigate this effect, we employ an isolation trench that etches the silicon oxide top cladding. For cross-section details and waveguide modelling, see Appendix A.
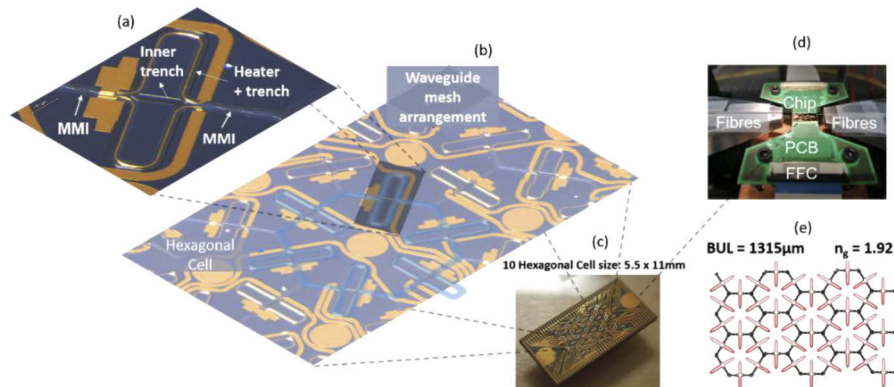

Fig. 1. (a) Labelled picture of the designed folded programmable unit cell, (b) labelled picture of the squeezed hexagonal cell, (c) picture of the 5.5×11 mm 40-cell chip, (d) electrically packaged chip on a Printed Circuit Board and setup with optical fibers and (e) schematic of the designed mesh.

We characterized the unit cell to obtain the main parameters that define its performance. First, the total Basic Unit Length (BUL) is 1297 μm and the group index is 1.923, resulting in a Basic Unit Delay of 8.4 ps approximately. This defines the minimum time discretization to synthetize interferometric structures. According to [27], our design will limit the free spectral range (FSR) of optical cavities (infinite impulse response filters) to 20, 12, 10, 8.58 GHz and the synthesis of Mach-Zehnder interferometers (finite impulse response filters) to FSRs of 60, 30, 20, 15, 12 GHz.

Next, we characterized the overall insertion loss of the PUC by measuring paths with different number of PUCs, resulting in 2 dB/PUC (See Fig. 2(a). This contribution is mainly due to the 3-dB MMI designs that result in 1dB/MMI, limiting the overall chip performance.
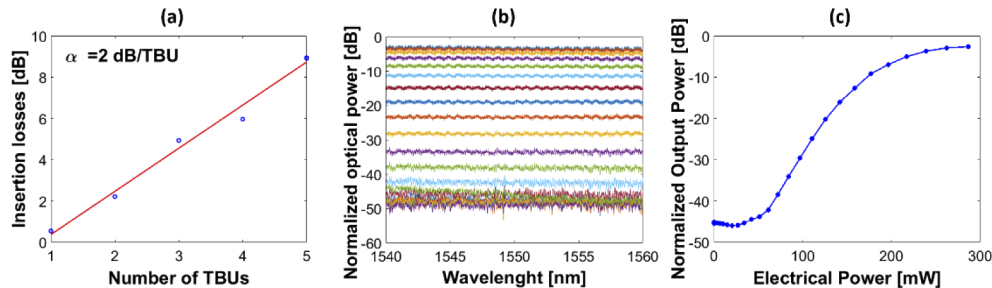

Fig. 2. (a) Measured paths with different number of PUCs, (b) Optical spectral response of one of the measured PUC measured with 1pm resolution and 10001 sampling points and normalized to a 11 mm straight waveguide for different electrical powers and (c) Normalized output power as a function of the applied electrical power.

Finally, we characterized the optical crosstalk and the power consumption, resulting in up to 45 dB and 290 mW/π, respectively (See Fig. 2(b) and 2(c). Optical spectral responses are normalized to the measured insertion losses corresponding to an 11mm integrated straight waveguide in the same chip. These losses include the input and output butt-coupling losses (from lensed MFD 2.5 μm fibers), the propagation losses and the setup losses, resulting in 12 dB approximately. In Fig. 2(b), we can see that a flat uniformity is maintained over a 20 nm range. Each trace corresponds to a different electrical driving condition up to 290 mW, where only one heater is employed. The electro-optical calibration of each phase shifter revealed that, in contrast to what was experienced in [3], the passive state of most of the unit cells is the theoretical cross-state, as it can be observed in Fig. 2(c). This behaviour corroborates the reduction of phase errors in silicon nitride platforms when compared to silicon on insulator platforms.

2.2. Waveguide mesh arrangement design

For the waveguide arrangement, we designed a 40-PUC hexagonal mesh, with 17 optical ports distributed between two opposite sides of the die. We designed the chip using Synopsys Optodesigner. The chip was integrated on a silicon nitride platform fabricated by the Centro Nacional de Microelectrónica in a CNM-VLC Photonics Multiproject Wafer Run. The chip waveguides provide 1.5 dB/cm propagation loss and the employed edge couplers show a 3.5 dB per coupler approximately [24,25].

Next, the chip was encapsulated and wirebondered to a PCB, as it is shown in Fig. 1(d). Since the available foundry technology stack, optimized for rapid prototyping, only allowed for 1 common metal layer for the heaters and the metal routing, the chip includes a ground layer and a routing scheme to enable the ground sharing employing metal pads and internal wire bonds.

For its operation, the PCB was fixed in temperature. However, small localized temperature variations produced fiber-coupling alignment issues which prevented us from employing dynamic programming methods [29–31]. We associated it to the material expansion due to the temperature

changes. We observed that a high temperature allowed us to achieve a relatively more stable behavior, so we fixed the chip temperature to 360C.

3.   Experimental results

Many different photonic integrated circuits including 1 and 2 input/output complex filters, dispersion compensator delay lines and universal interferometers, among others, can be implemented in a waveguide mesh [1–9]. To validate the performance of the folded-PUC arrangement, we focus on simple applications such as splitting, filtering and optical transmission, as examples of the broad applicability of general-purpose photonic meshes.

3.1.   Reconfigurable optical splitters

Optical splitters divide the signal among different paths with arbitrary optical power ratios. With a waveguide mesh arrangement, one can reconfigure the number of paths, and the splitting ratios by acting over each phase actuator to synthetize different optical splitting schemes [32]. As a basic demonstration example, we configured first a 1×2 3-dB optical splitter. Figure 3 illustrates the configuration scheme, and the location of the input and the output port, following unit cell representation given by their tunable coupling state. The overall path length results in 6 PUC. In a second example, illustrated in Fig. 4, we measured a 1×4 6-dB optical splitter. In this case, the overall path length results in 10 PUC. Note that having uneven light-path dimensions for each optical channel would result in a severe optical power deviation between optical outputs, given by the measured 2-dB/ PUC.
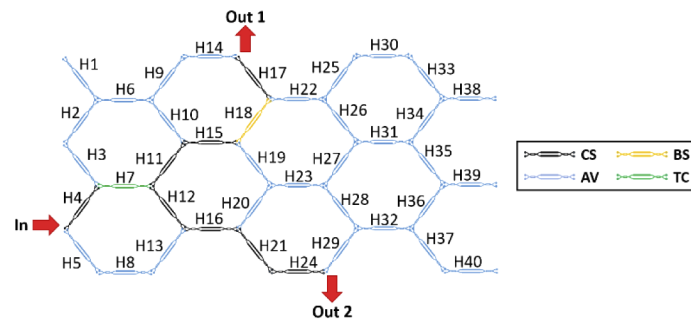

Fig. 3. Waveguide mesh connection diagram for the two outputs of the 1×2 synthetized optical splitter. CS: Cross state, BS: Bar state: TC: Tunable Coupler, AV: Available

Figure 5 represents the experimental results of each of the outputs for both 1×2 and 1×4 optical splitters. Optical spectral responses are normalized again to the measured insertion losses corresponding to an integrated straight waveguide in the same chip. As it can be gathered from Fig. 5, the total accumulated losses for the 1×2 and 1×4 splitters are around 15dB and 26dB respectively. These are in agreement with the expected losses for 6-PUC and 10-PUC paths, taking into account the insertion losses per PUC of 2dB obtained in the previous section and the splitter insertion losses of 3dB for the 1:2 case and 6dB for the 1×4 ones. Moreover, a flat response with a ±1dB deviation was obtained over the whole wavelength range of 20nm measured. Finally, taking into account the measured power consumption per PUC, the overall maximum electrical power consumption is 435mW and 580mW for the 1×2 and 1×4 splitters, respectively.

3.2.   Reconfigurable optical filters

As a second application demonstration, we programmed the circuit to perform a set of reconfigurable optical filters. The hexagonal interconnection topology enables single cavity optical ring
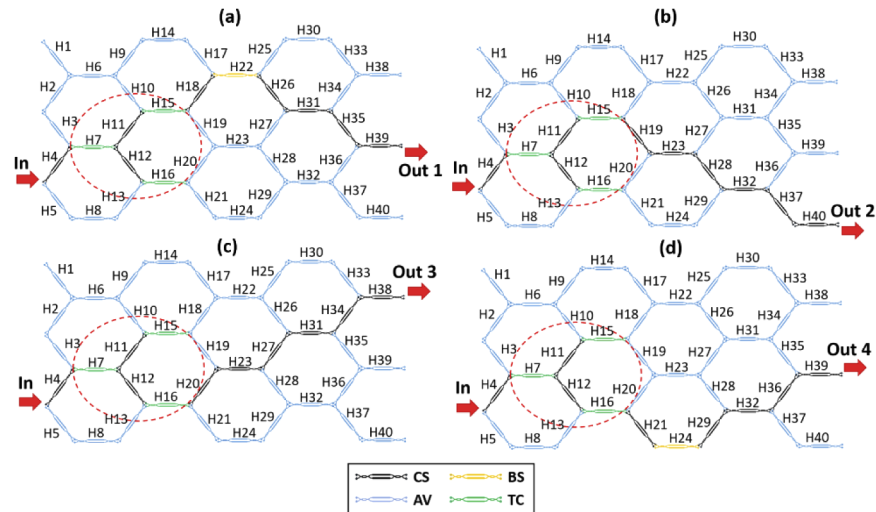
Fig. 4. Waveguide mesh connection diagram for the each of the four outputs of the 1×4 synthetized optical splitter. CS: Cross state, BS: Bar state: TC: Tunable Coupler, AV: Available
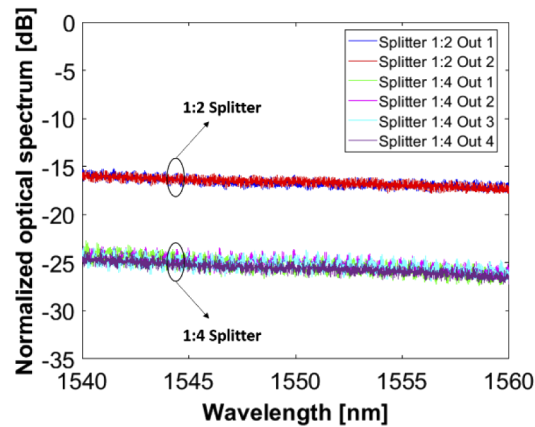

Fig. 5. Normalized optical output power measured for each output of the optical splitters.

resonators (ORRs) with cavity lengths given by 6, 10, 12, 14, 16 and 18 BULs [27]. Increasing the length of the cavity is limited by the accumulated loss. Figure 6 shows, the result for a 6-BUL (Fig. 6 top) and a 10-BUL (Fig. 6 bottom) cavity lengths ring resonator filters. Figure 6(a) shows the 40- unit cell hexagonal waveguide mesh configurations, where each unit cell is represented by a given colour depending on its tunable coupling state. Each measured optical spectrum is also shown. Again, measured spectral responses are normalized to the measured insertion losses corresponding to an integrated straight waveguide in the same chip. As it can be seen from Fig. 6(b), the synthetized 6-BUL ring resonator filter provides insertion losses of around 12 dB and an extinction ratio of 30 dB while the synthetized 10-BUL provides insertion losses of around 20 dB, as expected from the 2 dB/PUC results measured previously. The extinction ratio in this case is up to 30 dB although we observed a high variation due to the limited resolution of the optical spectrum analyzer. The resulting FSR was 0.16 nm (20 GHz) and 0.09 nm (12 GHz) for the 6-BUL and 10-BUL cases respectively, matching with the predicted value during

the design stage. Moreover, the overall maximum electrical power consumed by both 6-BUL and 10-BUL filters is 1595mW.
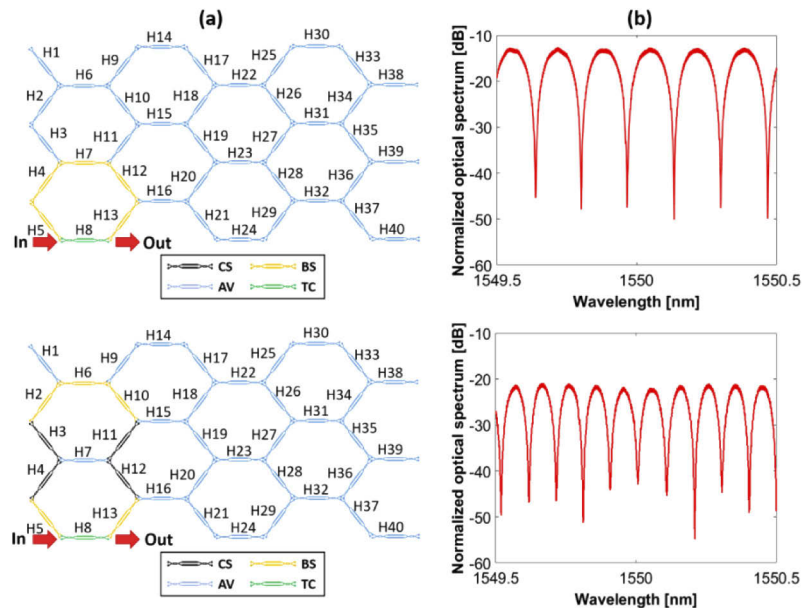

Fig. 6. Experimental results for the 6-BUL ORR (up) and 10-BUL ORR (down) optical filters. (a) Waveguide mesh connection diagrams, (b) measured optical transfer functions normalized to a straight waveguide. CS: Cross state, BS: Bar state: TC: Tunable Coupler, AV: Available

Continuing with optical filters, we synthetized a pair of unbalanced Mach Zehnder Interferometer (UMZI) filters. The hexagonal interconnection topology enables the configuration of MZI devices with path unbalances given by 0, 2, 4, 6 and 8. BULs [27]. Figure 7 shows two of the measured filters, related to a 2-BUL and a 4-BUL UMZIs. In the first case, the optical filter exhibits an extinction ratio up to 45 dB and insertion loss of 12 dB. In the second case, the filter shows insertion losses of 16 dB and an extinction ratio of 24 dB, mainly limited by the short tuning range of our heaters. The measured FSR was, as expected, 0.49 nm (60 GHz) for the 2-BUL case and 0.24 nm (30 GHz) for the 4-BUL ones. Finally, the overall maximum electrical power consumption measured is 870mW in the 2-BUL filter case and 1160mW in the 4-BUL filter ones.

3.3. Reconfigurable microwave photonic filters

RF-photonic signal filtering is probably the most widespread application in integrated MWP processors [2,33–35]. Specifically, the combination of a flexible reconfigurable optical cores and modulation and photodetection subsystems, enable the design of fully integrated tunable RF-photonic devices to meet flexible wideband spectral processing requirements for actual and future RF communication bands. As a basic validation example, we focus on microwave notch filters. Such a filter is crucial for removing interferences in dynamic, wideband radio systems, such as cognitive or ultra-wideband radios [33–35]. These applications demand high resolution filtering with a very high notch peak rejection.

When compared to application specific photonic circuits, the programmable processor suffers from extra excess losses due to the waveguide lattice mesh, reducing the total RF gain of the filter. To overcome this limitation, the integration of optical amplifiers in the system must be considered.
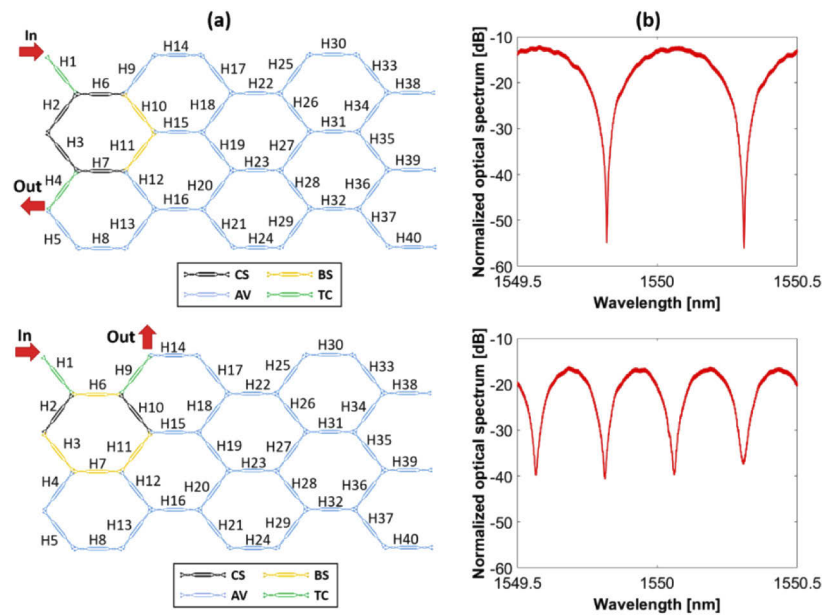
Fig. 7. Experimental results for UMZI optical filter of $\Delta L = 2$ BULs (up) and $\Delta L = 4$BULs (down). (a) Waveguide mesh connection diagrams, (b) Measured optical transfer functions normalized to a straight waveguide. CS: Cross state, BS: Bar state: TC: Tunable Coupler, AV: Available

On the other hand, the reconfigurability of the filter is enhanced, resulting in a more powerful and versatile device. Although the noise figure and the dynamic range could be deteriorated, the programmable processor could take advantage from its high-reconfigurability degree to perform optimum filtering and linearization over the whole system in the optical or in the RF domain.

To perform a microwave photonic filter, different modulation and detection schemes can be employed to increase the tunability range, the dynamic range, the gain and the noise figure of the whole system [35]. For validation purposes, we first set up a microwave photonic filter system using a double side-band (DSB) modulation to map the optical filter responses to the RF domain. The optical filters in this case correspond to the 6-BUL ORR and the 2-BUL UMZI examples of the previous section. The beating of the RF sidebands, and the carrier filtered by the optical filter define the RF filter shape.

A schematic diagram of the microwave photonic system experiment is presented in Fig. 8. First, an optical carrier emitted by a tunable laser source (TLS), and a vector network analyzer (PNA) is used to modulate the dual-drive MZM. This is biased at the optimum quadrature bias point (QB). The DSB modulated signal is amplified by an erbium-doped fiber amplifier (EDFA) and feeds the optical integrated filter by means of a lensed fiber and is afterwards collected at its output by another lensed fiber. Once the signal is outside the chip, it is split into two distinct paths by a 90/10 optical coupler (OC). The 10% signal is injected into an OSA while the other 90% is photodetected (PD) and sent to a microwave network analyzer (PNA).

Figure 9 shows the resulting RF filter shapes mapped with the 6-BUL ORR [Fig. 9(a)] and the 2-BUL UMZI [Fig. 9(b)] optical filters. Upper part of Fig. 9 shows the RF gain of the system. As it can be observed, microwave photonic notch filters with high peak rejection (40 dB approx.) are obtained. Lower part of Fig. 9 shows the RF filters responses normalized by the non-flat response of the system (modulator + EDFA + photodetector, without the optical filter), demonstrating
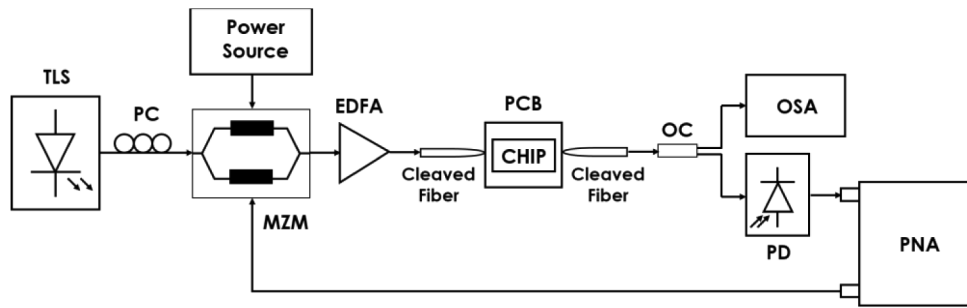
Fig. 8. Diagram of the experimental set-up used for the synthesis of the microwave filters.

that a modulator and photodetector with larger bandwidth is required to avoid the optical power degradation slope for higher frequencies.
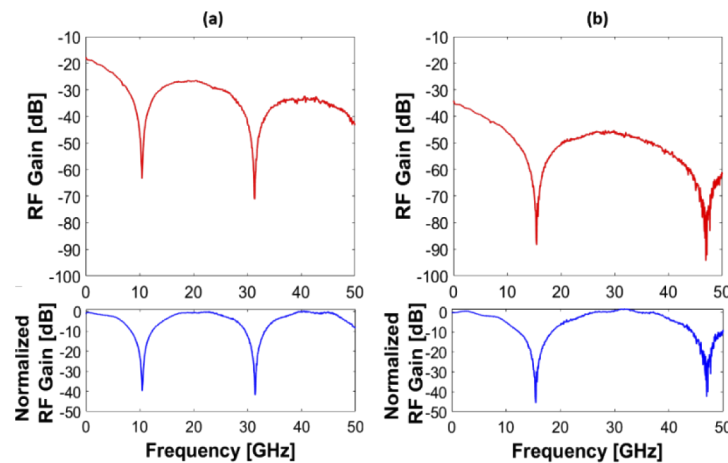

Fig. 9. Microwave photonic filter responses obtained from (a) the 6-BUL ORR optical filter and (b) UMZI ΔL=2BUL optical filter. Lower parts are the responses normalized to the modulator, the EDFA and the photodetector.

In order to demonstrate a tunable MWP filter, we require single-side band (SSB) modulation following the interconnection scheme shown at Fig. 10(a). In this case, we measured the tunability feature with three different schemes to obtain the SSB. Firstly, a dual-drive modulator (DD-MZM) Sumitomo T.DEH1.5-40-ADC was used with a RF- 90° hybrid [Fig. 10(b)]. Secondly, we employed the same dual-drive modulator in combination with a wave-shaper implementing a stop-band filter to mitigate one of the RF side-band, avoiding the use of the 90° hybrid [Fig. 10(c)]. Finally, to obtain the SSB in the third scheme, an in-phase and quadrature modulator (IQ-MZM) Photline MXIQ-LN-40 with a 90° hybrid was used, avoiding in this case the wave-shaper [Fig. 11(d)].

Before the MWP filter measurement, we characterized the SSB modulation employing a set of modulating RF frequencies ranging from 5 to 30 GHz for the case of DD-MZM [Fig. 11(a)] and IQ-MZM [Fig. 11(b)] both with a 90° hybrid. As it can be observed, almost total rejection between RF bands is obtained for the IQ-MZM in comparison with the DD-MZM + 900-Hybrid case, for which we measured a side-band rejection ranging from 6–8 dB. For the case of the DD-MZM + wave-shaper, total rejection of one RF side-band respect to the other is also obtained
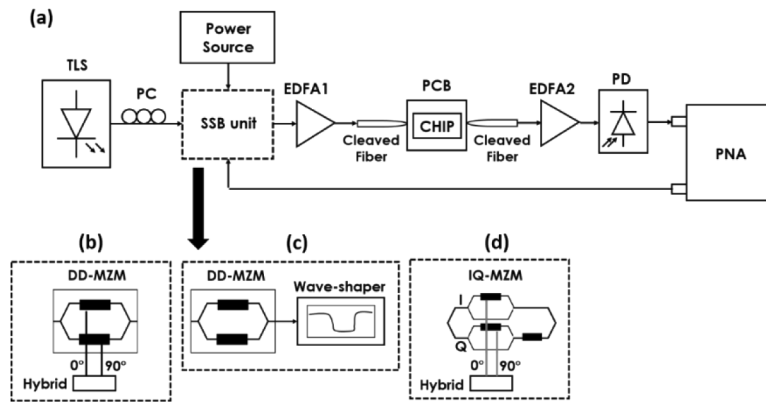
Fig. 10. (a) Diagram of the experimental set-up used for the tunability feature demonstration with SSB modulation by employing (b) a DD-MZM and a 90° hybrid, (c) a DD-MZM with a wave-shaper and (d) an IQ-MZM with a 90° hybrid.
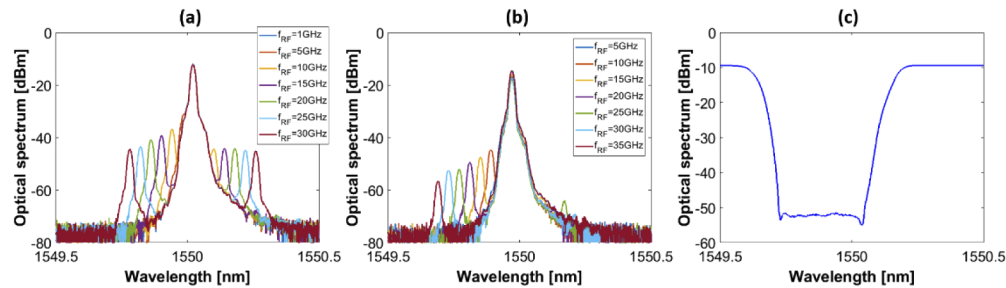

Fig. 11. Optical spectra of the SSB modulation implemented by (a) a DD-MZM with a 90° hybrid and (b) an IQ-MZM with a 90° hybrid. (c) Optical spectrum of the stop-band filter synthetized with the wave-shaper to filter the desired SSB.

by using an optical stop-band filter with the optical response shown in Fig. 11(c), synthetized by means of the wave-shaper.

By tuning the relative position of the carrier with respect to the spectral trace of the optical filter, we can induce the same tuning to the beating of the filtered RF sideband signal. Although this can be done tuning the spectral response of the filter, in this case the mechanism used to tune the MWP filter is the carrier wavelength sweeping. Figure 12 shows the tunability results obtained for the three schemes above presented. If the sideband suppression is worst, the resulting photodetected RF signal has non-negligible contributions of the beating between the undesired sideband and the optical carrier and between the undesired (mitigated) sideband and the targeted sidebands, both filtered by a non-symmetric optical filter response with respect to the optical carrier. This fact leads to a degradation of the translation of the optical filter to the RF domain that can be appreciated in the reduction of the extinction ratio, ripples, additional notches and uneven spectral responses. Overall, we obtained better performance in terms of the filter extinction ratio for the case of the DD-MZM + wave-shaper although for its operation, it requires the simultaneous tuning of the wave-shaper with the optical carrier. Note that in the three cases, the optical carrier is also filtered by an amount that depends on its relative position with respect to the optical filter. Since the main contribution to the RF photodetected power is the beating between the optical carrier and the RF sideband the passband optical loss varies with the tuning.
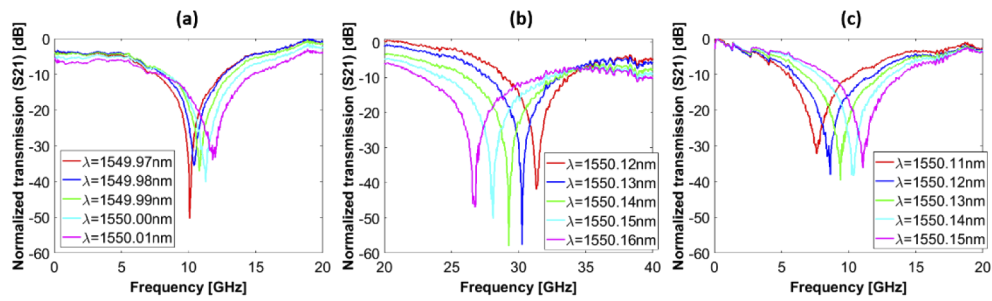
Fig. 12. MWP filter tunability feature by carrier wavelength shifting demonstrated employing (a) a DD-MZM and a 90° hybrid, (b) a DD-MZM with a wave-shaper and (c) an IQ-MZM with a 90° hybrid. Responses normalized to the modulator, the EDFA and the photodetector.

To mitigate this effect, an important class of MWP systems operates in the so-called self-beating mode that work on a self-homodyne fashion by sharing the same laser source for information bearing and local oscillator tasks [36]. As an application example, we also demonstrated the tunability of the MWP filter by using a self-beating based scheme as the one shown in Fig. 13(a). Two optical couplers (OC) were used at the input (90/10) and output (50/50) to implement the self-beating technique. Results of the MWP filter tunability by means of the carrier wavelength shifting are presented in Fig. 13(b).
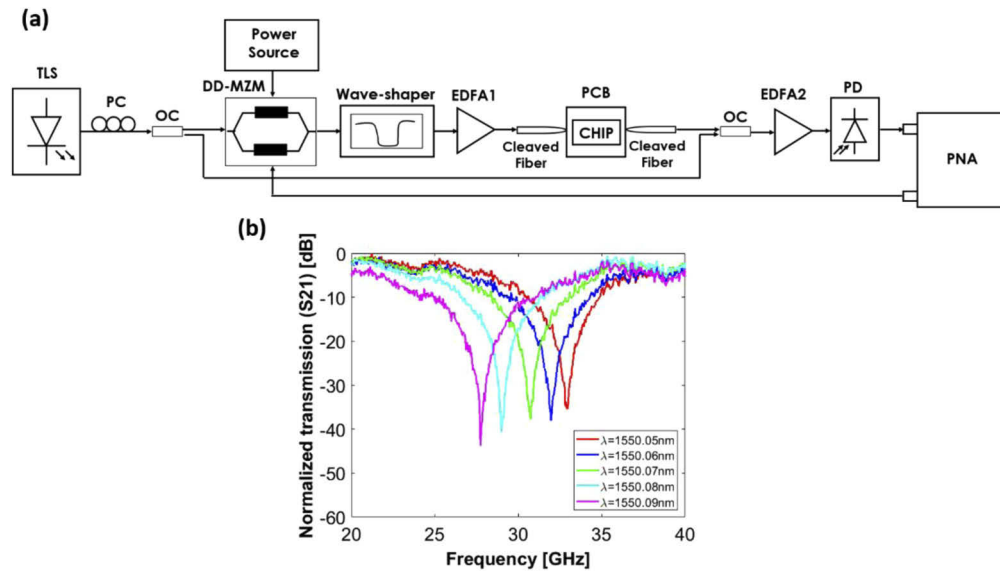

Fig. 13. (a) Experimental set-up used for the tunability feature demonstration with SSB modulation with self-beating effect by employing a DD-MZM with a wave-shaper and (b) MWP filter tunability feature by carrier wavelength shifting. Responses normalized to the modulator, the EDFA and the photodetector.

3.4. *Digital signal transmission*

As a final validation example, we analyze the usage of the SiN folded-PUC photonic mesh for the dynamic optical transmission/ routing of digitally modulated signals, opening the path to more complex tasks like smart signal processing and management in datacenters or radio-over

fiber and 5G communication centers [37–40]. For that purpose, we programmed the mesh to perform optical signal interconnection between optical paths with different path lengths. Next, we introduced 5G standard signals to be transmitted through the mesh. In order to measure the signal degradation, we employed a typical figure of merit to characterize MWP links, the error vector magnitude (EVM) which is measured at the receiver and gives a good indication of the signal quality. The EVM parameter is used in most wireless system standards such Wi-Fi or in mobile networks such as 5G, to calculate the performance of a transmitter/modulator or receiver/demodulator implementing the respective standard. It relates the performance of the actual waveform compared to an ideal signal as calculated over the course of the ideal constellation. Following the optical transmission, the lower EVM, the lower deterioration the signal will have suffered [41].

The setup used in this experiment is shown in Fig. 14. A vector signal generator (VSG) provides modulated signals that propagate through the optical chip before being photodetected and by an RF signal and spectrum analyzer (ESA). The modulated signals are time division duplex (TDD) new radio (NR) 5G signals with quadrature phase-shift keying (QPSK) and 64-quadrature amplitude modulated (64-QAM) modulation formats and 100 MHz bandwidth. Moreover, we used two frequencies within the two frequency ranges employed in the 5G NR technology. The first one is the Frequency Range 1 (FR1) which includes sub-6 GHz frequency band (f=5.9GHz) and the second is the Frequency Range 2 (FR2) including frequency bands in the mmWave range (f=26GHz).
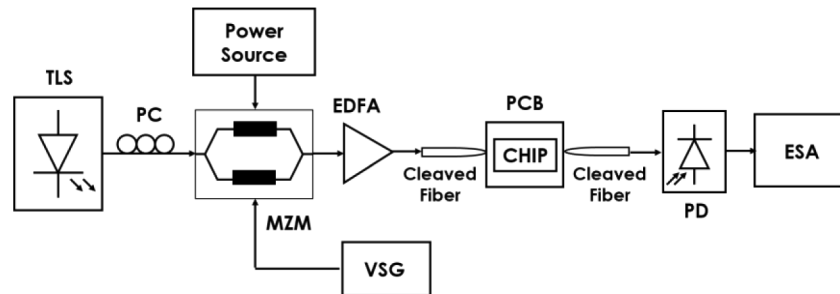

Fig. 14. Diagram of the experimental set-up used for the optical transmission of digital signals.

For the experiment we reconfigured the mesh to implement interconnection paths with different lengths (from 1 to 5 PUCs).

Figure 15 shows the received constellations of the QPSK (Fig. 15 top/left) and the 64-QAM modulated signals (Fig. 15 top/right) signals in the FR1 range, whereas constellations of the signals modulated at high frequency (FR2) are shown in the bottom part, QPSK in Fig. 15 bottom/left and 64-QAM in Fig. 15 bottom/right.

Finally, Fig. 15(b) shows the measured EVM for each transmitted signal as a function of the number of PUCs or TBUs crossed in the mesh. As it can be observed, the EVM is almost maintained along the increased number of TBUs, with an EVM around 1.34% for the FR1 signal (5.9GHz) and 2.1% for the FR2 signal (26GHz). These values are well below the allowed limit (3GPP TS 38.101-1 EVM requirements for different 5G modulation schemes: 17.5% for QPSK and 8% for 64-QAM, [42]), showing a high quality of the received signals and therefore the potential of the photonic mesh as a system enabling smart signal processing, routing and signal management of Radio-over-fiber signals.
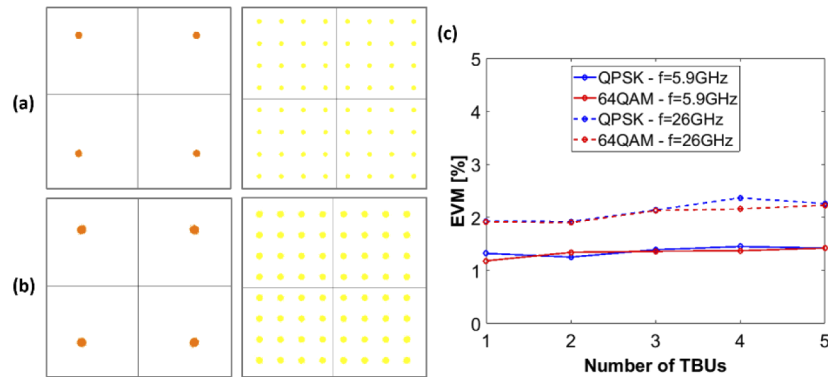
Fig. 15. Constellation diagrams corresponding to (a) FR1 frequency range and (b) FR2 frequency range (QPSK: left and 64-AQM: right). (c) Measured error vector magnitude as a function of the length of the path in the mesh in terms of number of crossed unit cells or TBUs.

4. Discussion

The roadmap for future scalable programmable photonic processors calls for improvements in insertion loss, fabrication tolerance, power consumption and integration density of the basic programmable unit cells to enable more flexible and versatile circuits. On this topic, a comparison between silicon and silicon nitride platforms suggests that silicon on insulator achieves better integration densities due to its higher confinement. This requirement is exacerbated for large scale circuits, where the maturity of the silicon platform is also better positioned [43]. However, the integrated optics technology is becoming more flexible thanks to the heterogeneous integration of both silicon and silicon nitride waveguides and the integration of suspended waveguide structures that allow the miniaturization and power efficiency improvement of phase actuators in both material platforms. Main scalability limits and issues of large scale programmable photonic circuits are discussed in [20,23,43].

Table 1 includes the main examples reported to date of reconfigurable waveguide mesh arrangements [43]. We can see that the integration density of the folded-heater PUC mesh improves by a factor of 2.8 compared with previously reported meshes in silicon nitride. In addition, it integrates a large number of 40 unit cells (80 phase actuators) in this material platform. In order to compare the folded-design with a non-folded design following the same interconnection pattern, we could compute that a similar unit-cell design with non-folded heaters of the hexagonal mesh would require a Unit Cell (MZI) longitudinal dimension of 1270 um compared to the 714 um of the current unit (MZI). Following a similar reasoning for the area analysis as the one followed in [27], the area of the hexagonal cell can be expressed in general as $A_{connected\_cell} = kPUC_{l-dim}^2$, where k = 1 for the square pattern, $k = 3\sqrt{3}/2$ for the hexagonal arrangement and $k = \sqrt{3}/4$ for the triangular arrangement, and PUC_{l-dim} is the longitudinal dimension of the programmable unit cell. Thus, a PUC_{l-dim} reduction ratio of 1.77 for the current example is translated to an area improvement of 3.13. On a general case, the area improvement is the square of the reduction ratio of the longitudinal dimension of the unit cell.

However, a major drawback of the reported chip is the limiting insertion loss per unit cell that reduces its applicability and scalability. This can be improved with the optimization and re-design of the 50:50 MMI couplers. For 3-dB couplers, two alternative architectures stand out: directional couplers and multimode interferometers. Several demonstrations of directional couplers in silicon nitride have revealed the requirement of larger footprint (around 350–400 um / coupler) [2]. In addition, directional couplers feature larger dispersive profiles limiting

Table 1. Comparison between reported waveguide mesh arrangements[a]

Year	Ref.	TBU	PS	OP	dB/TBU	BUL (um)	BUD (ps)	TE	Tech	P (mW)/pi	RT (us)	Top.	TBU	Size (mmxmm)	TBU density (1/mm2)	C (CL)
2015	[2]	7	14	4	TBD	3450	19.7	TO	Si3N4	300	TBD	Sq.	MZI	3.5×8.5	0.235	E (TBD)
2016	[3]	30	60	24	0.59	975	13.5	TO	SOI	110	TBD	Hex.	MZI	15×15	0.133	V (6.5)
2018	[23]	5	10	8	<0.13	1178	TBD	TO	Si3N4	300	TBD	Tri.	DD-DC	7×2.5	0.285	E (3.5)
2017–2020	This work	40	80	30	2.00	1315	8.4	TO	Si3N4	290	TBD	Hex.	MZI	11×5.5	0.661	E (3.5)

[a]TBU: Number of TBU, PS: Number of phase shifters, OP: Number of optical ports, BUL: Basic unit length, BUD: Basic unit delay, TE: Tuning effect, TO: Thermo-optic, P: Power consumption, RT: Response time, Top: Topology, C (CL): Fiber-chip coupling method (Losses in dB). E: Edge-coupling, V: Vertical-coupling. First in [41].

the bandwidth of interest. In contrast, MMI designs can be optimized and designed to improve the insertion loss up to 0.3 dB and imbalances of 0.2 dB on average while maintaining good conditions (IL<0.4 dB and uniformity) over 40 nm [44]. MMIs across platforms improve compactness, high fabrication tolerance, inherent output power balance, polarization insensitivity and lower optical loss, when compared to conventional directional couplers.

As an additional weakness, the integration platform and the resulting layer stack showed a non-stable thermo-expansive behaviour that prevent us from using automated programming routines [29–31]. This effect was translated in power drops of more than 8 dB on a straight waveguide characterization when tuning a set of heaters of the device. Indeed, since thermal expansion of the material is the most probable issue, a possible solution to this issue is to employ a fixed optical interfacing to the chip by gluing two optical fiber arrays using epoxy. In order to increase the integration density, a second metal layer would be required to provide an efficient opto-electronic phase actuation and mitigate the thermal expansion problem. In this chip, the intra-heater crosstalk given by the folded heater allowed us to reduce the heater dimension. However, we reached the miniaturization limit and a further reduction would produce a degradation of the heaters before achieving a 1800 phase shift [28].

From an integrated microwave photonic system perspective, more complex architectures can be exploited to produce fully tunable and reconfigurable MWP systems. This includes the use of alternative modulation-photodetection schemes and the configuration of alternative optical processing circuits [35]. The obtained RF gain values, even in the presence of one or two optical amplifiers, suggest the requirement for better modulator and photodetector performances, the need for integrated optical power amplification and in-line amplification, as well as the improvement of the overall chip loss.

Overall, although the reported performance is quite limited in terms of insertion loss, it is demonstrated the potential of the folded-heater PUC design as a path to achieve higher integration densities.

5. Conclusion

General-purpose programmable photonic processors rely on the large-scale integration of beamsplitters and reconfigurable phase shifters, distributed within unit cells or photonic gates. However, their future evolution calls for improvements including the integration density that can be achieved with current mesh topologies. In this work, we presented a unit cell topology design to increase the integration density of waveguide mesh arrangements based on folded Mach-Zehnder interferometers. We reported the design details of a 40-unit cell waveguide mesh integrated in an 11×5.5 mm. silicon nitride chip achieving the highest integration density reported to date for a general-purpose photonic processor. The chip is electrically interfaced to a PCB and to verify its performance, we reported examples of reconfigurable optical beamsplitters, optical filters, basic tunable microwave photonic filters with high peak rejection, as well as the dynamic interconnection and routing of 5G digitally modulated signals within the photonic mesh. Overall, the results reported calls for higher improvements in the hardware of general-purpose photonic processors and open the path to additional application scenarios such as microwave photonics and 5G signals management.

Appendix A. Waveguide modelling and cross-section details

For this design, we have obtained the basic waveguide properties by employing a commercial mode solver. For these simulations we employed the following material properties of silicon nitride and silicon oxide at a temperature of 25 0C, [24,25]:

$$n_{SiO_2}(\lambda) = \sqrt{\frac{1.09877\lambda^2}{\lambda^2 - 92.4317^2} + 1} \qquad n_{Si_3N_4}(\lambda) = \sqrt{\frac{2.8936\lambda^2}{\lambda^2 - 139.67^2} + 1}. \tag{1}$$

In our case, we have employed a deep waveguide with width w_{core} of 1 μm to satisfy the single-mode condition of the waveguide. This geometry has been widely employed in the previous Multi-Project Wafer Runs, [24]. Figure. 16(a) illustrates the waveguide cross-section.

From the mode-solver, we obtained the effective index data for a set of wavelength points illustrated in Fig. 16(b). We developed a compact model based on a second order Taylor series to perform a fitting of the data to obtain the corresponding values over the wavelength range between 1.5–1.6 μm. The resulting coefficients for the fundamental TE mode are given by Eq. (3):

$$n_{eff}(\lambda) = x_1 + x_2(\lambda - \lambda_0) + x_3(\lambda - \lambda_0)^2, \tag{2}$$
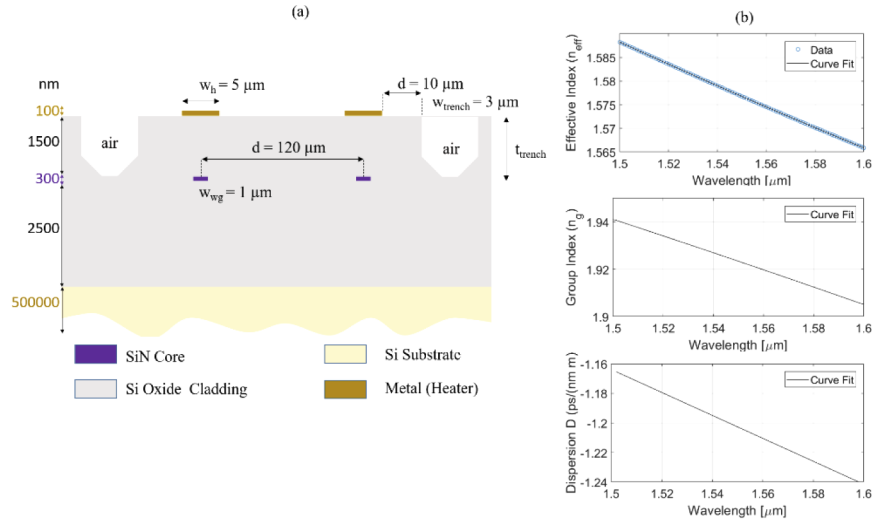
$$x_1 = 1.5767,$$

$$x_2 = -0.2236,$$

$$x_3 = 0.1163.$$

Fig. 16. (a) Waveguide cross-section, (b) obtained effective index, group index and dispersion characteristics for $w_{core} = 1$ μm.

These parameters can be straightforwardly translated to the group index and waveguide second-order dispersion coefficient as:

$$n_{eff}(\lambda_0) = x_1$$

$$n_g(\lambda) = n_{eff}(\lambda) - \lambda \frac{\partial n_{eff}(\lambda)}{\partial \lambda} = x_1 - x_2 \lambda_0 \tag{3}$$

$$D(\lambda) = -\frac{\lambda}{c} \frac{\partial^2 n_{eff}(\lambda)}{\partial \lambda^2} = -\frac{2\lambda}{c} x_3$$

where c is the speed of light in vacuum.

For the central wavelength, 1.55 μm, we have obtained an effective index of 1.5767, group index of 1.9234 and a second-order dispersion of -1.2027 ps/(nm·m). The effective thermo-optic coefficient ($\partial n / \partial Tc$) is 3.05×10^{-5} K^{-1} [28].

Disclosures. The authors declare no conflicts of interest.

References

1. D. Pérez, I. Gasulla, P. Das Mahapatra, and J. Capmany, "Principles, fundamentals, and applications of programmable integrated photonics," Adv. Opt. Photonics **12**(3), 709–786 (2020).
2. L. Zhuang, C. G. H. Roeloffzen, M. Hoekman, K.-J. Boller, and A. J. Lowery, "Programmable photonic signal processor chip for radiofrequency applications," Optica **2**(10), 854–859 (2015).
3. D. Pérez, I. Gasulla, L. Crudgington, D. J. Thomson, A. Z. Khokhar, K. Li, W. Cao, G. Z. Mashanovich, and J. Capmany, "Multipurpose silicon photonics signal processor core," Nat. Commun. **8**(1), 636 (2017).
4. D. A. B. Miller, "Perfect optics with imperfect components," Optica **2**(8), 747–750 (2015).
5. A. Ribeiro, A. Ruocco, L. Vanacker, and W. Bogaerts, "Demonstration of a 4×4 port universal linear circuit," Optica **3**(12), 1348–1357 (2016).
6. D. A. B. Miller, "Self-configuring universal linear optical component," Photonics Res. **1**(1), 1–15 (2013).
7. D. A. B. Miller, "Self-aligning universal beam coupler," Opt. Express **21**(5), 6360–6370 (2013).
8. M. Reck, A. Zeilinger, H. J. Bernstein, and P. Bertani, "Experimental realization of any discrete unitary operator," Phys. Rev. Lett. **73**(1), 58–61 (1994).
9. W. R. Clements, P. C. Humphreys, B. J. Metcalf, W. S. Kolthammer, and I. A. Walsmley, "Optimal design for universal multiport interferometers," Optica **3**(12), 1460–1465 (2016).
10. N. Harris, D. Bunandar, M. Pant, G. R. Steinbrecher, J. Mower, M. Prabhu, T. Baehr-Jones, M. Hochberg, and D. Englund, "Large-scale quantum photonic circuits in silicon," Nanophotonics **5**(3), 456–468 (2016).
11. J. Carolan, C. Harrold, C. Sparrow, E. Martín-López, N. J. Russell, J. W. Silverstone, P. J. Shadbolt, N. Matsuda, M. Oguma, M. Itoh, G. D. Marshall, M. G. Thompson, J. C. F. Matthews, T. Hashimoto, J. L. O'Brien, and A. Laing, "Universal linear optics," Science **349**(6249), 711–716 (2015).
12. J. Mower, N. C. Harris, G. R. Steinbrecher, Y. Lahini, and D. Englund, "High-fidelity quantum state evolution in imperfect photonic integrated circuits," Phys. Rev. A **92**(3), 032322 (2015).
13. N. C. Harris, J. Carolan, D. Bunandar, M. Prabhu, M. Hochberg, T. Baehr-Jones, M. L. Fanto, A. M. Smith, C. C. Tison, P. M. Alsing, and D. Englund, "Linear programmable nanophonic processor," Optica **5**(12), 1623–1631 (2018).
14. C. Taballione, T. A. W. Wolterink, J. Lugani, A. Eckstein, B. A. Bell, R. Grootjans, I. Visscher, J. J. Renema, D. Geskus, C. G. H. Roeloffzen, I. A. Walmsley, P. W. H. Pinkse, and K.-J. Boller, "8×8 programmable quantum photonic processor based on silicon nitride waveguides," in *Frontiers in Optics/Laser Science, OSA Technical Digest* (Optical Society of America, 2018), paper JTu3A.58 8.
15. H. Peng, M. A. Nahmias, T. F. de Lima, A. N. Tait, and B. J. Shastri, "Neuromorphic photonic integrated circuits," IEEE J. Sel. Top. Quantum Electron. **24**(6), 1–15 (2018).
16. P. R. Prucnal and B. J. Shastri, *Neuromorphic Photonics* (CRC Press, 2017).
17. Y. Shen, N. C. Harris, S. Skirlo, M. Prabhu, T. Baehr-Jones, M. Hochberg, X. Sun, S. Zhao, H. Larochelle, D. Englund, and M. Soljačić, "Deep learning with coherent nanophotonic circuits," Nat. Photonics **11**(7), 441–446 (2017).
18. A. Anoni, E. Guglielmi, M. Carminati, G. Ferrari, M. Sampietro, D. A. B. Miller, A. Melloni, and F. Morichetti, "Unscrambling light—automatically undoing strong mixing between modes," Light Sci. Appl. **6**(12), e17110 (2017).
19. L. N. Chen, E. Hall, L. Theogarajan, and J. Bowers, "Photonic switching for data center applications," IEEE Photonics J. **3**(5), 834–844 (2011).
20. J. Capmany, I. Gasulla, and D. Pérez, "Toward programmable microwave photonics processors," J. Lightwave Technol. **36**(2), 519–532 (2018).
21. C. G. H. Roeloffzen, L. Zhuang, C. Taddei, A. Leinse, R. G. Heideman, P. W. L. van Dijk, R. M. Oldenbeuving, D. A. I. Marpaung, M. Burla, and K.-J. Boller, "Silicon nitride microwave photonic circuits," Opt. Express **21**(19), 22937–22961 (2013).
22. D. Pérez, I. Gasulla, and J. Capmany, "Field-programmable photonic arrays," Opt. Express **26**(21), 27265–27278 (2018).
23. D. Pérez, A. M. Gutierrez, E. Sánchez, P. DasMahapatra, and J. Capmany, "Integrated photonic tunable basic units using dual-drive directional couplers," Opt. Express **27**(26), 38071–38086 (2019).
24. P. Muñoz, G. Micó, L. A. Bru, D. Pastor, D. Pérez, J. D. Doménech, J. Fernández, R. Baños, B. Gargallo, R. Alemany, A. M. Sánchez, J. M. Cirera, R. Mas, and C. Domínguez, "Silicon nitride photonic integration platforms for visible, near-infrared and mid-infrared applications," Sensors **17**(9), 2088 (2017).
25. P. Muñoz, P. W. L. van Dijk, D. Geuzebroek, M. Geiselmann, C. Domínguez, A. Stassen, J. D. Doménech, M. Zervas, A. Leinse, C. G. H. Roeloffzen, B. Gargallo, R. Banos, J. Fernández, G. Micó, L. A. Bru, and D. Pastor, "Foundry developments toward silicon nitride photonics from visible to the mid-infrared," IEEE J. Sel. Top. Quantum Electron. **25**(5), 1–13 (2019).
26. H. Nejadriahi, A. Friedman, R. Sharma, S. Pappert, Y. Fainman, and P. Yu, "Thermo-optic properties of silicon-rich silicon nitride for on-chip applications," Opt. Express **28**(17), 24951–24960 (2020).

27. D. Pérez, I. Gasulla, J. Capmany, and R. A. Soref, "Reconfigurable lattice mesh designs for programmable photonic processors," Opt. Express **24**(11), 12093–12106 (2016).

28. D. Pérez, J. F. Rocío Baños, J. D. Doménech, A. M. Sánchez, J. M. Cirera, R. Mas, J. Sánchez, S. Durán, E. Pardo, C. Domínguez, D. Pastor, J. Capmany, and P. Muñoz, "Thermal tuners on a Silicon Nitride platform, " arXiv preprint arXiv:1604.02958 (2016).

29. D. Pérez, "Programmable Integrated Silicon Photonics Waveguide Meshes: Optimized Designs and Control Algorithms," IEEE J. Sel. Top. Quantum Electron. **25**(6), 1–10 (2019).

30. A. López, D. Pérez, P. DasMahapatra, and J. Capmany, "Auto-routing algorithm for field-programmable photonic gate arrays," Opt. Express **28**(1), 737–752 (2020).

31. D. Pérez, A. López, P. DasMahapatra, and J. Capmany, "Multipurpose self-configuration of programmable photonic circuits," Nat. Commun. **11**(1), 6359 (2020).

32. D. Pérez, E. Sánchez, and J. Capmany, "Programmable True Time Delay Lines Using Integrated Waveguide Meshes," J. Lightwave Technol. **36**(19), 4591–4601 (2018).

33. D. Marpaung, B. Morrison, R. Pant, C. Roeloffzen, A. Leinse, M. Hoekman, R. Heideman, and B. J. Eggleton, "Si3N4 ring resonator-based microwave photonic notch filter with an ultrahigh peak rejection," Opt. Express **21**(20), 23286–23294 (2013).

34. Y. Liu, A. Choudhary, D. Marpaung, and B. Eggleton, "Integrated microwave photonic filters," Adv. Opt. Photonics **12**(2), 485–555 (2020).

35. O. Daulay, G. Liu, X. Guo, M. Eijkel, and D. Marpaung, "A Tutorial on Integrated Microwave Photonics Spectral Shaping," J. Lightwave Technol. **39**(3), 700–711 (2021).

36. D. Pérez, I. Gasulla, J. Capmany, J. S. Fandiño, P. Muñoz, and H. Alavi, "Figures of merit for self-beating filtered microwave photonic systems," Opt. Express **24**(9), 10087–10102 (2016).

37. R. Waterhouse and D. Novack, "Realizing 5G: Microwave photonics for 5G mobile wireless systems," IEEE Microwave **16**(8), 84–92 (2015).

38. X. Li, J. Yu, and G. K. Chang, "Photonics-assisted technologies for extreme broadband 5G wireless communications," J. Lightwave Technol. **37**(12), 2851–2865 (2019).

39. A. Muniz, R. M. Borges, R. N. Da Silva, D. F. Noque, and A. Cerqueira, "Ultra-broadband photonics-based RF front-end toward 5G networks," J. Opt. Commun. Netw. **8**(11), B35–B42 (2016).

40. G. Serafino, C. Porzi, F. Falconi, S. Pinna, M. Puleri, A. D'Errico, A. Bogoni, and P. Ghelf, "Photonics-assisted beamforming for 5G communications," IEEE Photonics Technol. Lett. **30**(21), 1826–1829 (2018).

41. R. Schmogrow, B. Nebendahl, M. Winter, A. Josten, D. Hillerkuss, S. Koenig, J. Meyer, M. Dreschmann, M. Huebner, C. Koos, J. Becker, W. Freude, and J. Leuthold, "Error Vector Magnitude as a Performance Measure for Advanced Modulation Formats," IEEE Photonics Technol. Lett. **24**(1), 61–63 (2012).

42. . ETSI TS 138 521-1 V15.1.0 (2019-04), "User Equipment (UE) conformance specification; Radio transmission and reception".

43. J. Capmany and D. Pérez, *Programmable Integrated Photonics*, Oxford University Press, (2020).

44. J. Fernandez, J. Felip, J. Serrano, R. Caroselli, B. Gargallo, D. Domenech, and P. Muñoz, "Statistical analysis of passive components manufactured in a thick silicon nitride platform," at *European Conference on integrated Optics (ECIO 2020)*, Paris, France (2020).